Draft version February 1, 2022
Typeset using LaTeX **twocolumn** style in AASTeX631

Schwarzschild and Ledoux are equivalent on evolutionary timescales

Evan H. Anders,[1,2] Adam S. Jermyn,[3,2] Daniel Lecoanet,[1,4,2] Adrian E. Fraser,[5,2] Imogen G. Cresswell,[6,2] and J. R. Fuentes[7]

[1] CIERA, Northwestern University, Evanston IL 60201, USA
[2] Kavli Institute for Theoretical Physics, University of California, Santa Barbara, CA 93106, USA
[3] Center for Computational Astrophysics, Flatiron Institute, New York, NY 10010, USA
[4] Department of Engineering Sciences and Applied Mathematics, Northwestern University, Evanston IL 60208, USA
[5] University of California, Santa Cruz, Santa Cruz, California 95064, U.S.A
[6] Department Astrophysical and Planetary Sciences & LASP, University of Colorado, Boulder, CO 80309, USA
[7] Department of Physics and McGill Space Institute, McGill University, 3600 rue University, Montreal, QC H3A 2T8, Canada

(Received July 28, 2021; Revised October 19, 2021; Accepted; Published)

Submitted to ApJ

ABSTRACT

In stars, the location of convective boundaries is determined by either the Schwarzschild or Ledoux criterion, but there is not consensus among the 1D stellar modeling community over which criterion to use. In this letter we present a 3D hydrodynamical simulation of a convection zone whose boundary is stabilized by a composition gradient despite being thermally unstable. This convective boundary is Ledoux stable but Schwarzschild unstable. Over hundreds of convective overturn timescales, mixing at the convective boundary causes the convection zone to grow. The convection zone stops growing once it reaches a height where its boundary is stable by the Schwarzschild criterion. This work provides 3D evidence that convective boundaries which are Ledoux stable are fragile unless they are also Schwarzschild stable. Therefore, the Schwarzschild stability criterion properly describes the size of a convection zone, except for when convection zones do not reach statistically stationary states during short-lived evolutionary stages.

Keywords: Stellar convection zones (301), Stellar physics (1621); Stellar evolutionary models (2046)

1. INTRODUCTION

Observations tell us we don't understand the mixing at convective boundaries. For example, models and observations disagree about the sizes of convective cores (Claret & Torres 2018; Viani & Basu 2020; Pedersen et al. 2021), lithium abundances in solar-type stars (Pinsonneault 1997; Sestito & Randich 2005; Carlos et al. 2019; Dumont et al. 2021), and there is a well-known acoustic glitch in helioseismology at the base of the convection zone (see Basu 2016, Sec. 7.2.1). Improperly calculating the size of a convection zone can have important impacts across astrophysics such as setting the mass of stellar remnants (Farmer et al. 2019; Mehta et al. 2022) and affecting the inferred radii of exoplanets (Basu et al. 2012; Morrell 2020).

Corresponding author: Evan H. Anders
evan.anders@northwestern.edu

While there are many undercertainties in convective boundary mixing (CBM), the most fundamental question is: what sets the nominal boundary of the convection zone? One way of answering this question is by evaluating the *Schwarzschild criterion*, which determines where the temperature and pressure stratification within a star are stable or unstable. The other answer is the *Ledoux criterion*, which accounts for stability or instability due to the composition (e.g., the variation of helium abundance with pressure; see Salaris & Cassisi 2017, chapter 3, for a nice review of these criteria). Recent work states that these criteria are logically equivalent at a convective boundary in the mixing length formalism (Gabriel et al. 2014; Paxton et al. 2018, 2019), but they are not always implemented to be that way (as in early versions of the MESA instrument, Paxton et al. 2013).

Modern studies still have not reached a consensus of which criterion to employ (see Kaiser et al. 2020, chapter 2, for a brief discussion). Multi-dimensional simulations have demonstrated that convection zones with Ledoux-stable boundaries expand by entraining compositionally-stable regions (Meakin & Arnett 2007; Woodward et al. 2015; Jones et al. 2017; Cristini et al. 2019; Fuentes & Cumming 2020; Andrassy et al. 2020, 2021). However, it is unclear from past 3D simulations whether that entrainment should stop at a Schwarzschild-stable boundary, leading to uncertainty in how to model entrainment in 1D models (Staritsin 2013; Scott et al. 2021).

In this work, we present a simple 3D hydrodynamical simulation that demonstrates that convection zones with Ledoux-stable but Schwarzschild-unstable boundaries will entrain material over roughly a thermal timescale until both the Ledoux and Schwarzschild criteria are equivalent at the convective boundary. Therefore, in 1D stellar evolution models, when the evolution time is greater than or roughly equal to the thermal time (such as on the main sequence, see Georgy et al. 2021), these criteria should be implemented so that either one produces the same evolution. We briefly discuss these criteria in Sec. 2, display our simulations in Sec. **??**, and provide a brief discussion in Sec. 4.

2. THEORY & EXPERIMENT

The stability of a convective region can instantaneously be determined using the Schwarzschild criterion,

$$\mathcal{Y}_{\mathrm{S}} = \nabla_{\mathrm{rad}} - \nabla_{\mathrm{ad}}, \tag{1}$$

or the Ledoux criterion,

$$\mathcal{Y}_{\mathrm{L}} = \mathcal{Y}_{\mathrm{S}} + \frac{\chi_\mu}{\chi_T}\nabla_\mu \tag{2}$$

Here, the temperature gradient $\nabla \equiv d\ln P/d\ln T$ has a value of ∇_{ad} for an adiabatic stratification and ∇_{rad} if all flux is carried through radiative conductivity. The composition gradient $\nabla_\mu = d\ln\mu/d\ln P$ is multiplied by the ratio of $\chi_T = (d\ln P/d\ln T)_{\rho,\mu}$ and $\chi_\mu = (d\ln P/d\ln\mu)_{\rho,T}$, where ρ is the density, T is the temperature, P is the pressure, and μ is the mean molecular weight.

In Eqns. 1 and 2, $\mathcal{Y}$ is the discriminant (e.g., Paxton et al. 2018, sec. 2), related to the superadiabaticity. In stellar structure codes, convective boundaries are assumed to coincide with sign changes in the discriminant. The various stability regimes which can occur in stars are well-described in section 3 and figure 3 of Salaris & Cassisi (2017), but we will briefly recap four important regimes:

1. Convection Zones (CZs): If $\mathcal{Y}_{\mathrm{S}} > 0$ and $\mathcal{Y}_{\mathrm{L}} \geq \mathcal{Y}_{\mathrm{S}}$, a region's stratification is convectively unstable.
2. Radiative Zones (RZs): If both $\mathcal{Y}_{\mathrm{S}} < 0$ and $\mathcal{Y}_{\mathrm{L}} < \mathcal{Y}_{\mathrm{S}}$, a region's stratification is stable to convection.
3. "Semiconvection" zone: If $\mathcal{Y}_{\mathrm{S}} > 0$ but $\mathcal{Y}_{\mathrm{L}} < 0$, a stable composition gradient stabilizes an unstable thermal stratification. These regions can be linearly unstable to overstable doubly diffusive convection (ODDC, see Garaud 2018, chapter 2), or they can be stable RZs.
4. "Thermohaline" zone: If $\mathcal{Y}_{\mathrm{S}} < 0$ and $\mathcal{Y}_{\mathrm{L}} > \mathcal{Y}_{\mathrm{S}}$, a stable thermal stratification stabilizes an unstable composition gradient. These regions can be linearly unstable to thermohaline mixing or fingering convection (see Garaud 2018, chapter 3), or they can be stable RZs.

In this paper, we study 3D simulations of a linearly-stable semiconvection zone (#3) bounded below by a CZ (#1) and above by an RZ (#2). We examine how the boundary of the CZ evolves through entrainment. In particular, we are interested in seeing if $\mathcal{Y}_{\mathrm{S}}$ and $\mathcal{Y}_{\mathrm{L}}$ evolve towards the same height due to entrainment. Since stellar evolution timesteps generally span many convective overturn times, our 3D simulation should evolve to the proper state, which may be quite different from our initial conditions.

In this work, we utilize a simplified 3D model which employs the Boussinesq approximation, which assumes that the depth of the layer being studied is much smaller than the local scale height. Since we are studying thin regions near convective boundaries, this assumption is OK. The relevant physics for this problem are included (∇_{rad} varies with height, buoyancy is determined both by the composition C and the temperature stratification T), so $\mathcal{Y}_{\mathrm{S}}$ and $\mathcal{Y}_{\mathrm{L}}$ are meaningfuly defined and distinct from one another when composition gradients are present. For details on our model setup and Dedalus simulations, we refer the reader to appendices A and B.

3. RESULTS

Volume visualizations of the composition field in our simulation are shown near the initial state (left) and evolved state (right) in Fig. 1. While our domain spans $z = [0, 3]$, we only plot $z = [0, 2.5]$ to focus on the interesting regions. We furthermore plot horizontal lines which correspond to the roots of $\mathcal{Y}_{\mathrm{L}}$ (orange) and $\mathcal{Y}_{\mathrm{S}}$ (purple). Initially, the bottom third of the domain is a CZ ($\mathcal{Y}_{\mathrm{L}} > 0$ and $\mathcal{Y}_{\mathrm{S}} > 0$), the middle third is a semi-convection zone ($\mathcal{Y}_{\mathrm{L}} < 0$ but $\mathcal{Y}_{\mathrm{S}} > 0$), and the top third is an RZ ($\mathcal{Y}_{\mathrm{L}} \leq \mathcal{Y}_{\mathrm{S}}$, $\mathcal{Y}_{\mathrm{S}} < 0$). Note that we observe

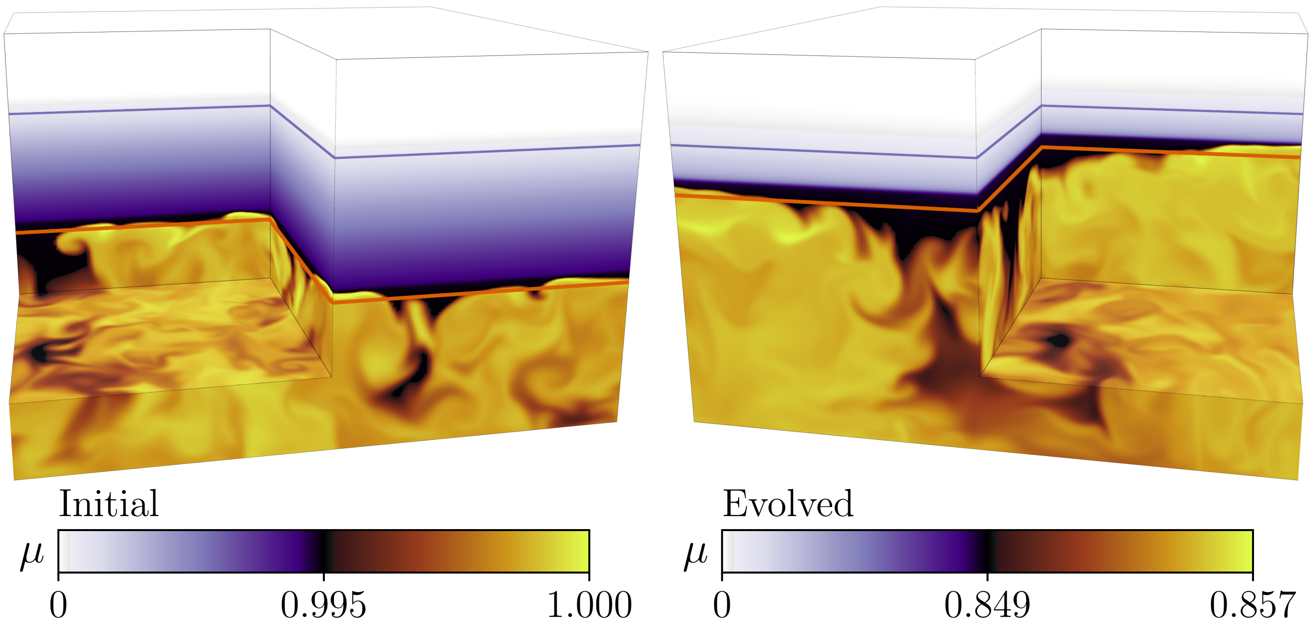

Figure 1. Volume renderings of the composition field μ in our simulation at early (left) and late (right) times. The change in color from white to dark purple from the top of the box to the top of the convection zone denotes a stable composition gradient. The convection zone is mostly well-mixed, so we expand the colorbar scaling there; black represents entrained low-composition fluid being mixed into the yellow high-composition convection zone. The orange and purple horizontal lines respectively denote the roots of the Ledoux and Schwarzschild discriminants (Eqns. 1 & 2). Note: this is currently evolving further so that the last sentence isn't a lie.

mechanical overshoot at all times: convective velocities are nonzero a small but appreciable distance above the $\mathcal{Y}_\mathrm{L} = 0$ line. This occurs because the root of the discriminant denotes where the sign change occurs in the buoyant acceleration, not where the convective velocity is zero.

The most obvious difference between the panels on the left and the right is that the CZ has consumed the semiconvection zone and fills the bottom two-thirds of the box. Convective flows which overshot the convective boundary entrained low-composition material from the stable layer into the convection zone. Convective motions mixed this fluid, and this process repeated over thousands of convective overturn times until the Ledoux and Schwarzschild boundaries of the convection zone coincided. At this point, the convection zone ceased its expansion, and the *thermal* stability of the Schwarzschild-stable RZ was sufficient to halt expansion of the convection zone.

Figure 2 displays vertical profiles from our simulation in the initial (left) and evolved (right) states. Shown are the composition μ (top), the discriminants $\mathcal{Y}_\mathrm{L}$ and $\mathcal{Y}_\mathrm{S}$ (middle), and the square Brunt-Väisälä frequency (top) as well as the square convective frequency defined as

$$f_\mathrm{conv}^2 = \frac{|\boldsymbol{u}|^2}{L_\mathrm{conv}^2}, \tag{3}$$

where $\boldsymbol{u}$ is the velocity and L_conv is the depth of the convectively unstable layer.

Initially, the composition is uniform in the CZ ($z \leq 1$) and RZ ($z \geq 2$), but varies linearly in the semiconvection zone $z \in [1, 2]$. The root of $\mathcal{Y}_\mathrm{L}$ occurs at $z \approx 1$ while that of $\mathcal{Y}_\mathrm{S}$ occurs at $z \approx 2$. Finally, initially $f_\mathrm{conv}^2 = 0$ because we start in a stationary state. The Brunt-Väisälä frequency N^2 is negative in a boundary layer at the base of the CZ which drives the instability. N^2 is stable for $z \gtrsim 1$, and is larger in the RZ than the semiconvection zone by an order of magnitude[1]

The evolved state is attained after convection entrains and mixes the stabilizing fluid in the semiconvection zone. We see that the composition profile (top) is constant in the convection zone, and approximates a step function at the top of the overshoot zone. The roots of the discriminants $\mathcal{Y}_\mathrm{L}$ and $\mathcal{Y}_\mathrm{S}$ coincide (middle). Furthermore, in the CZ, the convective frequency is roughly constant and $N^2 \lesssim 0$. In the RZ, $f_\mathrm{conv}^2 \approx 0$ and $N^2 \gg 0$. We can compute the "stiffness" of the

[1] We ran simulations where N^2 was identical in the RZ and semiconvection zone and saw similar behavior. We make N^2 large in the RZ to reduce overshoot in the evolved state.

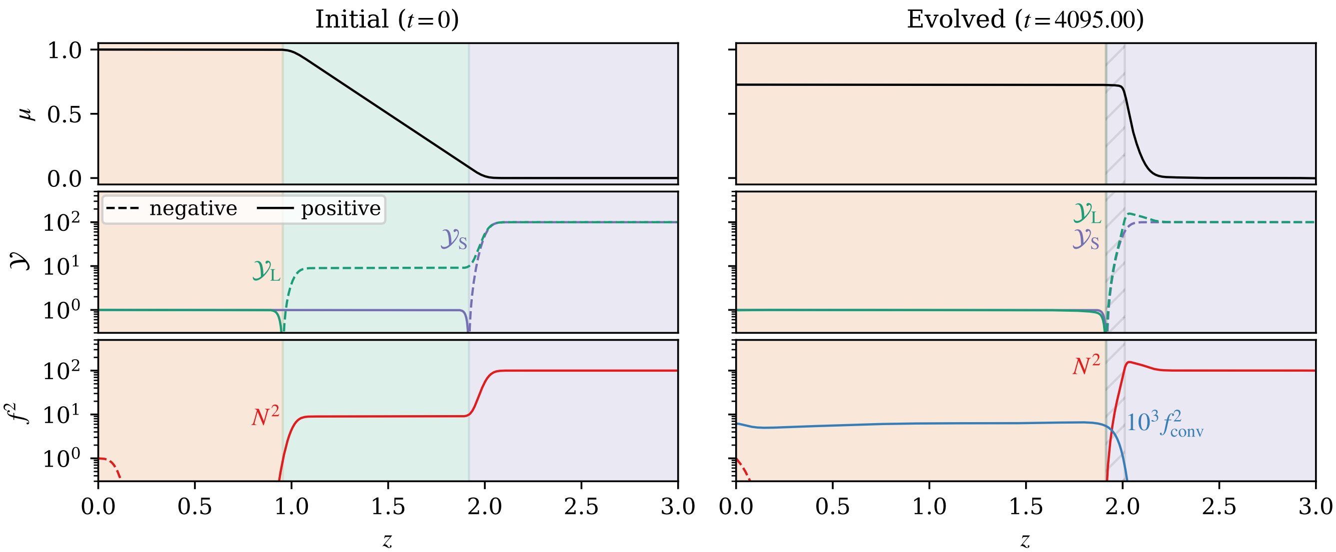

Figure 2. Horizontally-averaged profiles are shown for the composition (top), the discriminants $\mathcal{Y}_\mathrm{S}$ and $\mathcal{Y}_\mathrm{L}$ (middle, Eqns. 1 & 2), and the Brunt-Väisälä frequency $N^2 = -\mathcal{Y}_\mathrm{L}$ and the square convective frequency f^2_conv (bottom, Eqn. 3), where $\boldsymbol{u}$ is the velocity and L_conv is the depth of the convection zone. Positive values are solid lines and negative values are dashed lines. We show the initial (left) and evolved (right, time-averaged over 100 convective overturn times) states. The background color is orange in CZs, green in semiconvection zones, and purple in RZs per Section 2. The lightly hashed background region in the evolved RZ is where mechanical overshoot occurs. Note: this data is taken from a less turbulent run than fig 1; it'll be updated when the fig 1 run finishes.

radiative-convective interface,

$$\mathcal{S} = \frac{N^2|_\mathrm{RZ}}{f^2_\mathrm{conv}|_\mathrm{CZ}}, \tag{4}$$

which is related to the oft-studied Richardson number. In our evolved simulation, we measure $\mathcal{S} \sim 10^4$. Boundaries with a low stiffness $\mathcal{S} \lesssim 10$ easily deform in the presence of convective flows, but convective boundaries in stars often have $\mathcal{S} \gtrsim 10^6$. The value of $\mathcal{S}$ achieved in these simulations is therefore in the right regime to study entrainment at a stellar convective boundary.

Finally, in Figure 3, we plot a Kippenhahn-like diagram of the simulation's height vs. time to show evolutionary trends. The roots of $\mathcal{Y}_\mathrm{L}$ and $\mathcal{Y}_\mathrm{S}$ are respectively shown as orange and purple lines. The CZ is colored orange and sits below the root of $\mathcal{Y}_\mathrm{L}$, the RZ is colored purple and sits above the root of $\mathcal{Y}_\mathrm{S}$, and the semiconvection zone is colored green and sits between the roots. Convection motions "overshoot" above the root of $\mathcal{Y}_\mathrm{L}$. The height where the horizontally-averaged kinetic energy falls below 10% of its bulk-CZ value is marked with a black line, and the hashed region below it is the overshoot zone. We note that the black line and overshoot zone roughly correspond with the maximum of $\partial\mu/\partial z$ (Fig. 2, upper right), so this is a good description. Importantly, note that the lines tracing $\mathcal{Y}_\mathrm{L} = 0$ and $\mathcal{Y}_\mathrm{S} = 0$ start at different heights, but 3D convective mixing makes these lines converge on long timescales.

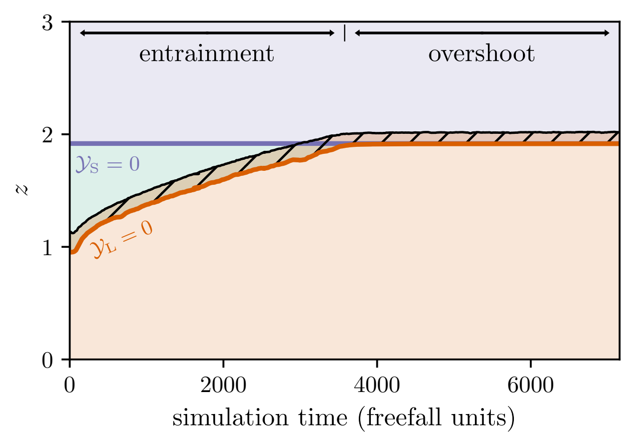

Figure 3. A kippenhahn-like diagram of the evolution of our simulation. The orange line denotes the Ledoux boundary ($\mathcal{Y}_\mathrm{L} = 0$); the CZ is below this and is colored orange. The purple line denotes the Schwarzschild boundary ($\mathcal{Y}_\mathrm{S} = 0$); the RZ is above this and is colored purple. The semiconvective region with $\mathcal{Y}_\mathrm{S} > 0$ and $\mathcal{Y}_\mathrm{L} < 0$ is colored green. The black line denotes the top of the hashed overshoot zone. The simulation has an "entrainment phase" while the CZ expands, and a pure "overshoot phase" where the convective boundary does not advance. Note: this data is taken from a less turbulent run than fig 1; it'll be updated when the fig 1 run finishes.

4. CONCLUSIONS & DISCUSSION

In this letter, we present 3D simulations of a convection zone and its boundary. The initial boundary is compositionally stable but weakly thermally unstable (Ledoux stable but Schwarzschild unstable). Entrainment causes the convective boundary to advance until the Ledoux and Schwarzschild criterion agree upon the location of the convective boundary.

These simulations demonstrate that the Ledoux criterion properly defines the *instantaneous* criterion for the boundary of a convection zone. However, when the evolutionary timescale $t_{\rm evolution} \gg t_{\rm conv}$, the convective overturn timescale, the Schwarzschild criterion provides the best description of the steady-state boundary of the convection zone. Our 3D dynamical simulations support the claim that "logically consistent" implementations of mixing length theory (Gabriel et al. 2014; Paxton et al. 2018, 2019) must set the Schwarzschild discriminant $\mathcal{Y}_{\rm S} = 0$ at the convective boundary. This suggests that the MESA software instrument's modern "convective pre-mixing" (CPM) algorithm should properly find the boundary of most convection zones. Put differently, our simulations suggest that 1D stellar evolution models should not produce different answers when using the Schwarzschild or Ledoux criterion for convective stability when $t_{\rm evolution} \gg t_{\rm conv}$.

We note briefly that many Ledoux-stable but Schwarzschild-unstable regions in stars are unstable to overstable doubly-diffusive convection (ODDC). ODDC generally mixes more quickly than the entrainment studied here, and has been studied extensively in local simulations (Mirouh et al. 2012; Wood et al. 2013; Xie et al. 2017); see Garaud (2018) for a nice review. ODDC has been applied in 1D stellar evolution models to the regions near main sequence stellar convective cores in Moore & Garaud (2016). They find rapid mixing of ledoux-stable but schwarzschild-unstable regions, and ODDC formulations should should be widely included in stellar models.

For stages in stellar evolution where $t_{\rm conv} \sim t_{\rm evolution}$, implementations of time-dependent convection (TDC, e.g., Kuhfuss 1986) should be employed to properly capture convective dynamics and the advancement of convective boundaries. The advancement of convective boundaries in TDC implementations should be informed by time-dependent theories and simulations of the motion of convective boundaries (e.g., Turner 1968; Fuentes & Cumming 2020).

The purpose of this study was to understand how the root of the discriminant $\mathcal{Y}_{\rm L}$ evolves over time, and whether it coincides with the root of $\mathcal{Y}_{\rm S}$ at late times. While there is interesting behavior near the boundary beyond that point (e.g., mechanical convective overshoot), a detailed analysis of that phenomenon is beyond the scope of this work. We furthermore constructed the simulations in this work to have a small penetration parameter $\mathcal{P}$ (**?**) and we see negliglble convective penetration in our simulations. Finally, in our simulations, the radiative conductivity is independent of the magnitude of the composition μ, but this is not the case in stars. Since the radiative conductivity sets the location of the Schwarzschild boundary, including these effects would change the exact location of our final convective boundary, but would not change the fundamental takeaways of this work.

In summary, we find that the Schwarzschild criterion provides the location of the convective boundary in a statistically stationary state; in this final state, the Ledoux and Schwarzschild criteria are degenerate.

We thank Meridith Joyce, Anne Thoul, Dominic Bowman, Jared Goldberg, Tim Cunningham, Falk Herwig, Kyle Augustson, (OTHERS?) for useful discussions which helped improve our understanding. EHA is funded as a CIERA Postdoctoral fellow and would like to thank CIERA and Northwestern University. This research was supported in part by the National Science Foundation under Grant No. PHY-1748958, and we acknowledge the hospitality of KITP during the Probes of Transport in Stars Program. Computations were conducted with support from the NASA High End Computing (HEC) Program through the NASA Advanced Supercomputing (NAS) Division at Ames Research Center on Pleiades with allocation GID s2276. The Flatiron Institute is supported by the Simons Foundation.

APPENDIX

A. MODEL & INITIAL CONDITIONS

In this work we study the simplest possible system: incompressible, Boussinesq convection with a composition field and a height-varying background radiative conductivity, similar to that used in Fuentes & Cumming (2020) and Anders et al. (2021). These equations are

$$\boldsymbol{\nabla} \cdot \boldsymbol{u} = 0 \tag{A1}$$

$$\partial_t \boldsymbol{u} + \boldsymbol{u} \cdot \boldsymbol{\nabla} \boldsymbol{u} + \boldsymbol{\nabla} \varpi = \left(T - \frac{\mu}{\mathrm{R}_0}\right) \hat{z} + \frac{\mathrm{Pr}}{\mathcal{P}} \boldsymbol{\nabla}^2 \boldsymbol{u}, \tag{A2}$$

$$\partial_t T + \boldsymbol{u} \cdot \boldsymbol{\nabla} T + w \boldsymbol{\nabla}_{\rm ad} + \boldsymbol{\nabla} \cdot [-\kappa_{T,0} \boldsymbol{\nabla} \overline{T}] = \frac{1}{\mathcal{P}} \boldsymbol{\nabla}^2 T', \tag{A3}$$

$$\partial_t \mu + \boldsymbol{u}\cdot\boldsymbol{\nabla}\mu = -\frac{\tau_0}{\mathcal{P}}\boldsymbol{\nabla}^2\overline{\mu} + \frac{\tau}{\mathcal{P}}\boldsymbol{\nabla}^2\mu'. \quad \text{(A4)}$$

Here, $\boldsymbol{u}$ is the nondimensional velocity, T is the nondimensional temperature, and μ is the nondimensional concentration. Bars (e.g., $\overline{T}$) represent the horizontally-averaged component of a field and primes (e.g., T') denote all fluctuations around that background. The nondimensional control parameters are

$$\mathcal{P} = \frac{u_{\rm ff} L_{\rm conv}}{\kappa_T}, \qquad \mathrm{R}_0 = \frac{|\alpha|\Delta T}{|\beta|\Delta\mu}, \\ \mathrm{Pr} = \frac{\nu}{\kappa_T}, \qquad \tau = \frac{\kappa_\mu}{\kappa_T}, \quad \text{(A5)}$$

where the nondimensional freefall velocity is $\boldsymbol{u}_{\rm ff} = \sqrt{|\alpha| g L_{\rm conv}\Delta T}$ with g the constant gravitational acceleration, $L_{\rm conv}$ is the initial depth of the convection zone, $\Delta\mu$ is the composition change across the Ledoux stable region, $\Delta T = L_{\rm conv}(\partial_z T_{\rm rad} - \partial_z T_{\rm ad})$ is the superadiabatic temperature scale of the convection zone, α and β are the coefficients of expansion for T and μ, ν is the viscosity, κ_T is the thermal diffusivity, and κ_μ is the compositional diffusivity. We also specify different values of $\kappa_T = \kappa_{T,0}$ and $\kappa_\mu/\kappa_T = \tau_0$ for the horizontally-averaged component; this allows the radiative gradient to change with height and reduces diffusion on the mean μ structure to ensure evolution is due to advection. These equations are described in detail in Sec. 2 of Garaud (2018), except for the differing diffusivities on the averages and fluctuations.

We define the Ledoux and Schwarzschild discriminants

$$\mathcal{Y}_{\rm S} = \left(\frac{\partial T}{\partial z}\right)_{\rm rad} - \left(\frac{\partial T}{\partial z}\right)_{\rm ad}, \; \mathcal{Y}_{\rm L} = \mathcal{Y}_{\rm S} - \mathrm{R}_0^{-1}\frac{\partial\mu}{\partial z}, \quad \text{(A6)}$$

and in this nondimensional system the Brunt-Väisälä frequency is the negative of the Ledoux discriminant $N^2 = -\mathcal{Y}_{\rm L}$.

In this work, we study a three-layer model in $z = [0, 3]$,

$$\left(\frac{\partial T}{\partial z}\right)_{\rm rad} = \left(\frac{\partial T}{\partial z}\right)_{\rm ad} + \begin{cases} -1 & z \le 2 \\ 10\mathrm{R}_0^{-1} & z > 2 \end{cases}, \quad \text{(A7)}$$

$$\frac{\partial\mu_0}{\partial z} = \begin{cases} 0 & z \le 1 \\ -1 & 1 < z \le 2 \\ 0 & 2 < z \end{cases}, \quad \text{(A8)}$$

where the intial temperature derivative is $\partial T_0/\partial z = (\partial T/\partial z)_{\rm rad}$ everywhere except between $z = [0.1, 1]$ where it is adiabatic. We set $(\partial T/\partial z)\mathrm{ad} = -1 - 10\mathrm{R}_0^{-1}$.

B. SIMULATION DETAILS & DATA AVAILABILITY

We time-evolve equations A1-A4 using the Dedalus pseudospectral solver (Burns et al. 2020) using timestepper SBDF2 (Wang & Ruuth 2008) and safety factor 0.3. All variables are spectral expansions of Chebyshev coefficients in the vertical (z) direction ($n_z = 512$ between $z = [0, 2.25]$ plus $n_z = 64$ between $z = [2.25, 3]$) and as $(n_x, n_y) = (192, 192)$ Fourier coefficients in the horizontally periodic (x, y) directions. Our domain spans $x \in [0, L_x]$, $y \in [0, L_y]$, and $z \in [0, L_z]$ with $L_x = L_y = 4$ and $L_z = 3$. To avoid aliasing errors, we use the 3/2-dealiasing rule in all directions. To start our simulations, we add random noise temperature perturbations with a magnitude of 10^{-6} to the initial temperature profile.

Spectral methods with finite coefficient expansions cannot capture true discontinuities. In order to approximate discontinuous functions such as Eqns. A7 & A8, we define a smooth Heaviside step function centered at $z = z_0$,

$$H(z; z_0, d_w) = \frac{1}{2}\left(1 + \mathrm{erf}\left[\frac{z - z_0}{d_w}\right]\right). \quad \text{(B9)}$$

where erf is the error function and we set $d_w = 0.05$. The simulation in this work uses $\mathcal{P} = 3.2 \times 10^3$, $\mathrm{R}_0^{-1} = 10$, $\mathrm{Pr} = \tau = 0.5$, $\tau_0 = 1.5^{-3}$, and $\kappa_{T,0} = \mathcal{P}^{-1}[(\partial T/\partial z)_{\rm rad}|_{z=0}]/(\partial T/\partial z)_{\rm rad}$

We produce figures 2 and 3 using matplotlib (Hunter 2007; Caswell et al. 2021). We produce figure 1 using plotly (Inc. 2015) and matplotlib. All of the Python scripts used to run the simulations in this paper and to create the figures in this paper are publicly available in a git repository[2], and in a Zenodo repository (**?**).

[2] https://github.com/evanhanders/schwarzschild_or_ledoux

REFERENCES

Anders, E. H., Jermyn, A. S., Lecoanet, D., & Brown, B. P. 2021, arXiv e-prints, arXiv:2110.11356. https://arxiv.org/abs/2110.11356

Andrassy, R., Herwig, F., Woodward, P., & Ritter, C. 2020, MNRAS, 491, 972, doi: 10.1093/mnras/stz2952

Andrassy, R., Higl, J., Mao, H., et al. 2021, arXiv e-prints, arXiv:2111.01165. https://arxiv.org/abs/2111.01165

Basu, S. 2016, Living Reviews in Solar Physics, 13, 2, doi: 10.1007/s41116-016-0003-4

Basu, S., Verner, G. A., Chaplin, W. J., & Elsworth, Y. 2012, ApJ, 746, 76, doi: 10.1088/0004-637X/746/1/76

Burns, K. J., Vasil, G. M., Oishi, J. S., Lecoanet, D., & Brown, B. P. 2020, Physical Review Research, 2, 023068, doi: 10.1103/PhysRevResearch.2.023068

Carlos, M., Meléndez, J., Spina, L., et al. 2019, MNRAS, 485, 4052, doi: 10.1093/mnras/stz681

Caswell, T. A., Droettboom, M., Lee, A., et al. 2021, matplotlib/matplotlib: REL: v3.3.4, v3.3.4, Zenodo, doi: 10.5281/zenodo.4475376

Claret, A., & Torres, G. 2018, ApJ, 859, 100, doi: 10.3847/1538-4357/aabd35

Cristini, A., Hirschi, R., Meakin, C., et al. 2019, MNRAS, 484, 4645, doi: 10.1093/mnras/stz312

Dumont, T., Palacios, A., Charbonnel, C., et al. 2021, A&A, 646, A48, doi: 10.1051/0004-6361/202039515

Farmer, R., Renzo, M., de Mink, S. E., Marchant, P., & Justham, S. 2019, ApJ, 887, 53, doi: 10.3847/1538-4357/ab518b

Fuentes, J. R., & Cumming, A. 2020, Physical Review Fluids, 5, 124501, doi: 10.1103/PhysRevFluids.5.124501

Gabriel, M., Noels, A., Montalbán, J., & Miglio, A. 2014, A&A, 569, A63, doi: 10.1051/0004-6361/201423442

Garaud, P. 2018, Annual Review of Fluid Mechanics, 50, 275, doi: 10.1146/annurev-fluid-122316-045234

Georgy, C., Saio, H., & Meynet, G. 2021, A&A, 650, A128, doi: 10.1051/0004-6361/202040105

Hunter, J. D. 2007, Computing in Science and Engineering, 9, 90, doi: 10.1109/MCSE.2007.55

Inc., P. T. 2015, Collaborative data science, Montreal, QC: Plotly Technologies Inc. https://plot.ly

Jones, S., Andrassy, R., Sandalski, S., et al. 2017, MNRAS, 465, 2991, doi: 10.1093/mnras/stw2783

Kaiser, E. A., Hirschi, R., Arnett, W. D., et al. 2020, MNRAS, 496, 1967, doi: 10.1093/mnras/staa1595

Kuhfuss, R. 1986, A&A, 160, 116

Meakin, C. A., & Arnett, D. 2007, ApJ, 667, 448, doi: 10.1086/520318

Mehta, A. K., Buonanno, A., Gair, J., et al. 2022, ApJ, 924, 39, doi: 10.3847/1538-4357/ac3130

Mirouh, G. M., Garaud, P., Stellmach, S., Traxler, A. L., & Wood, T. S. 2012, ApJ, 750, 61, doi: 10.1088/0004-637X/750/1/61

Moore, K., & Garaud, P. 2016, ApJ, 817, 54, doi: 10.3847/0004-637X/817/1/54

Morrell, S. A. F. 2020, PhD thesis, University of Exeter

Paxton, B., Cantiello, M., Arras, P., et al. 2013, ApJS, 208, 4, doi: 10.1088/0067-0049/208/1/4

Paxton, B., Schwab, J., Bauer, E. B., et al. 2018, ApJS, 234, 34, doi: 10.3847/1538-4365/aaa5a8

Paxton, B., Smolec, R., Schwab, J., et al. 2019, ApJS, 243, 10, doi: 10.3847/1538-4365/ab2241

Pedersen, M. G., Aerts, C., Pápics, P. I., et al. 2021, arXiv e-prints, arXiv:2105.04533. https://arxiv.org/abs/2105.04533

Pinsonneault, M. 1997, ARA&A, 35, 557, doi: 10.1146/annurev.astro.35.1.557

Salaris, M., & Cassisi, S. 2017, Royal Society Open Science, 4, 170192, doi: 10.1098/rsos.170192

Scott, L. J. A., Hirschi, R., Georgy, C., et al. 2021, MNRAS, 503, 4208, doi: 10.1093/mnras/stab752

Sestito, P., & Randich, S. 2005, A&A, 442, 615, doi: 10.1051/0004-6361:20053482

Staritsin, E. I. 2013, Astronomy Reports, 57, 380, doi: 10.1134/S1063772913050089

Turner, J. S. 1968, Journal of Fluid Mechanics, 33, 183, doi: 10.1017/S0022112068002442

Viani, L. S., & Basu, S. 2020, ApJ, 904, 22, doi: 10.3847/1538-4357/abba17

Wang, D., & Ruuth, S. J. 2008, Journal of Computational Mathematics, 26, 838. http://www.jstor.org/stable/43693484

Wood, T. S., Garaud, P., & Stellmach, S. 2013, ApJ, 768, 157, doi: 10.1088/0004-637X/768/2/157

Woodward, P. R., Herwig, F., & Lin, P.-H. 2015, ApJ, 798, 49, doi: 10.1088/0004-637X/798/1/49

Xie, J.-H., Miquel, B., Julien, K., & Knobloch, E. 2017, Fluids, 2, doi: 10.3390/fluids2010006